# Printed Magnetic FePt Nanocrystal Films

**Reken N. Patel,[†,‡,§] Andrew T. Heitsch,[†,‡,§] Changbae Hyun,[∥] Detlef-M. Smilgies,[⊥] Alex de Lozanne,[∥,#] Yueh-Lin Loo,[*,¶] and Brian A. Korgel[*,†,‡,§]**

Department of Chemical Engineering, Center for Nano- and Molecular Science and Technology, Texas Materials Institute, and Department of Physics, The University of Texas at Austin, Austin, Texas 78712, Cornell High Energy Synchrotron Source (CHESS), Cornell University, Ithaca, New York 14853, and Department of Chemical Engineering, Princeton University, Princeton, New Jersey 08554

**ABSTRACT** Patterned monolayers and multilayers of FePt nanocrystals were printed onto substrates by first assembling nanocrystals on a Langmuir–Blodgett (LB) trough and then lifting them onto prepatterned polydimethylsiloxane (PDMS) stamps, followed by transfer printing onto the substrate. Patterned features, including micrometer-size circles, lines, and squares, could be printed using this approach. The magnetic properties of the printed nanocrystal films were also measured using magnetic force microscopy (MFM). Room-temperature MFM could detect a remanent (permanent) magnetization from multilayer (>3 nanocrystals thick) films of chemically ordered $L1_0$ FePt nanocrystals.

**KEYWORDS:** Langmuir–Blodgett • stamping • magnetic nanocrystals • iron platinum • magnetic force microscopy • magnetic memory

## INTRODUCTION

New materials systems are needed to meet the demand of 1 terabit in$^{-2}$ magnetic memory storage media (1, 2). Magnetic colloidal nanocrystals are an interesting possibility for this purpose, as they can be synthesized in large quantities with diameters less than 10 nm and processed using low-temperature deposition methods such as inkjet printing (3), spraying (4), or stamping (5–10). Due to their small size, however, most nanocrystals are superparamagnetic and susceptible to room-temperature thermal fluctuations that switch magnetic orientation and cause data loss (11). Therefore, only nanocrystals of materials with hard magnetic properties (i.e., high $BH_{max}$) such as compositionally ordered FePt and CoPt can exhibit the magnetic stability needed for long-term data storage (12, 13). The synthesis of nanocrystals of these types of materials is now well established (14–17), but deposition methods for these nanocrystals on substrates and an understanding of their magnetic properties is not.

For magnetic memory storage applications, the material must exhibit a sufficient magnetic field for detection. The magnetic field from individual nanocrystals is too weak to be detected using current technologies; therefore, functional magnetic "bits" must be composed of many nanocrystals, and these bits must be deposited with controlled position on a substrate. Various approaches to patterned nanocrystal deposition exist, including chemical surface tethering (18, 19), block copolymer templating (20), and electrostatic deposition (21), but they tend to be slow, requiring multiple fabrication steps, and often fail to provide uniform substrate coverage over large areas. One of the most reliable and straightforward methods to deposit uniform monolayers of nanocrystals is to use a Langmuir–Blodgett (LB) trough. Hydrophobic nanocrystals are assembled at the air–water interface of the LB trough and then transferred by dipping a substrate into the densely packed film. Wafer-scale deposition of uniform monolayers of nanocrystalline materials, ranging from nanowires to spherical nanocrystals, has been assembled in this way (22–28). Patterned arrays of nanocrystals have also been transferred by dipping a patterned polydimethylsiloxane (PDMS) stamp and then pressing the stamp onto a substrate to transfer the nanocrystals (5–8). Such patterns typically have micrometer scale dimensions. New fabrication techniques, however, have yielded PDMS stamps with nanometer-scale features (29).

Here, we demonstrate the patterned deposition of uniform monolayers and multilayers with a controlled thickness of FePt nanocrystals using a combination of LB assembly and PDMS stamp transfer and printing. The optimal conditions for obtaining monolayers of hexagonal close-packed nanoparticles are described. Both ligand-coated FePt nanocrystals and silica-coated FePt nanocrystals were studied. The as-prepared FePt nanocrystals are chemically disordered with weak magnetic properties and must be annealed at high temperature (>550°C) to obtain the chemically ordered $L1_0$ FePt phase. Printed FePt nanocrystal films were also annealed, and their magnetic properties were measured. The permanent magnetization of multilayer $L1_0$ FePt nanocrystal

* To whom correspondence should be addressed. B.A.K.: e-mail, korgel@che.utexas.edu; tel, 512-471-5633; fax, 512-471-7060. Y.-L.L.: e-mail, lloo@Princeton.edu; tel, 609-258-9091; fax, 609-258-0211.
Received for review April 6, 2009 and accepted April 21, 2009
† Department of Chemical Engineering, The University of Texas at Austin.
‡ Center for Nano- and Molecular Science and Technology, The University of Texas at Austin.
§ Texas Materials Institute, The University of Texas at Austin.
∥ Department of Physics, The University of Texas at Austin.
⊥ CHESS, Cornell University.
# Center for Nano- and Molecular Science and Technology.
¶ Department of Chemical Engineering, Princeton University.
DOI: 10.1021/am900237d

films was detectable by room-temperature magnetic force microscopy (MFM).

## EXPERIMENTAL DETAILS

**Materials and Supplies.** Platinum acetylacetonate ($Pt(acac)_2$, 97%), iron pentacarbonyl ($Fe(CO)_5$, 99.999%), oleylamine (70%), oleic acid (99%), Igepal CO-520, tetraethyl orthosilicate (TEOS, 98%), and octadecyltrimethoxysilane (OTMOS, 90%) were purchased from Sigma-Aldrich. Ethanol (ACS grade), acetone (ACS grade), 2-propanol (ACS grade), and chloroform (ACS grade) were purchased from Fisher Scientific. Dioctyl ether (>97%) and cyclohexane (ACS grade) were purchased from Fluka. Ammonium hydroxide ($NH_4OH$, 30% aqueous solution) was purchased from EMD Chemicals. (Tridecafluoro-1,1,2,2-tetrahydrooctyl)-1-trichlorosilane was purchased from Gelest. PDMS (Dow Corning, Sylgard 184) was purchased from EIS Inc. All chemicals were used as received. Deionized water (DI-$H_2O$) was used in all aqueous preparations. High-purity nitrogen and forming gas (7% $H_2$, 93% $N_2$) were purchased from Matheson Trigas.

**FePt Nanocrystal Synthesis.** FePt nanocrystals were synthesized using standard Schlenk line techniques, as reported elsewhere in the literature (14). In a typical reaction, 0.5 mmol (0.192 g) of $Pt(acac)_2$ was mixed with 10 mL of dioctyl ether in a three-neck flask. The flask was connected to the Schlenk line manifold, and the mixture was degassed by cycling nitrogen and pulling vacuum three times within a 1 h period at 45 °C. The headspace of the flask was refilled with nitrogen, and the mixture was heated to 120 °C. A 1.15 mmol (0.15 mL) portion of $Fe(CO)_5$, 4.4 mmol (1.45 mL) of oleylamine, and 4.25 mmol (1.35 mL) of oleic acid were sequentially injected through a septum into the solution. The temperature was increased at a heating rate of 15 °C $min^{-1}$ to 240 °C and the mixture incubated for 1 h. After incubation, the reaction mixture was refluxed at ~297 °C for an additional 1 h before removing the heating mantle and cooling the solution to room temperature. A 5 mL portion of chloroform was added to the nanocrystal product, and this mixture was subsequently transferred into a 50 mL centrifuge tube. Initial centrifugation at 8000 rpm for 5 min rid the nanocrystal product of uncapped or large chunks of nanocrystals. The precipitate was discarded, and ~15 mL of ethanol was added until the supernatant became turbid (indicating flocculation of nanocrystals). The turbid solution was centrifuged at 8000 rpm for 5 min, and a transparent supernatant was achieved. The supernatant was discarded, and the precipitated nanocrystals on the sides of the centrifuge tube were redispersed in 2 mL of chloroform. A 2−4 mL portion of ethanol was added to reprecipitate the nanocrystals from solution via centrifuging at 8000 rpm for 5 min. The solvent/antisolvent washing step was repeated twice to remove any excess ligands. The final FePt nanocrystal precipitate was redispersed in chloroform at a concentration of 10 mg $mL^{-1}$. The Fe:Pt composition of the nanocrystals determined by energy dispersive X-ray spectroscopy (EDS) elemental analysis was 42:57. Half of the FePt nanocrystals were separated to be coated with silica shells.

**$SiO_2$ Coating of FePt Nanocrystals.** FePt nanocrystals were coated with silica shells as described previously (30). A 10 mL portion of a 1 mg $mL^{-1}$ dispersion of FePt nanocrystals in cyclohexane was added to a solution of 6 mL of Igepal CO-520 in 100 mL of cyclohexane. A 0.65 mL portion of an aqueous 30 vol % $NH_4OH$ solution was added dropwise, followed by the addition of 1.0 mL of TEOS. The mixture was stirred for 72 h, upon which it was transferred to a separatory funnel. A 30 mL portion of ethanol was added to the solution, and separation between a cyclohexane-rich phase and ethanol-rich phase began. The FePt@$SiO_2$ nanoparticle transferred to the ethanol-rich phase. The cyclohexane was discarded, and the ethanol solution was connected to a rotary evaporator and ethanol was evaporated until ~10 mL of solution was left. The nanoparticles were then isolated by centrifugation at 8000 rpm for 5 min and redispersed in 5 mL of ethanol.

The FePt@$SiO_2$ nanoparticles were surface-modified with OTMOS by following procedures described by Wang et al. (31). A 10 mg portion of FePt@$SiO_2$ nanoparticles was mixed with 0.1 mL of 30 vol % $NH_4OH$ (aq) in 10 mL of ethanol. A 0.5 mL portion of 10 vol % OTMOS in chloroform was added dropwise to this solution and stirred for 24 h. The nanoparticles were isolated by centrifugation of the mixture at 8000 rpm for 5 min. The precipitate was redispersed in 2 mL of chloroform. A 4 mL portion of ethanol was added to the FePt@$SiO_2$ chloroform solution to flocculate the nanoparticles. The solution was centrifuged at 8000 rpm for 5 min, which precipitated the FePt@$SiO_2$ nanoparticles on the side wall of the centrifuge tube. The clear supernatant was discarded, and the chloroform/ethanol washing step was repeated two more times before finally redispersing the nanoparticles in chloroform.

**PDMS Stamp Fabrication.** PDMS stamps were fabricated by following the procedure previously described by Kumar et al. (32). PDMS molds were fabricated on silicon wafers using an AZ photoresist and conventional photolithography techniques. The lithography mask used contained arrays of lines, dots, and squares ranging in size from 1.5 to 20 $\mu$m (Toppan photomasks). Silanization of the photoresist surface was done by vacuum-depositing (tridecafluoro-1,1,2,2-tetrahydrooctyl)-1-trichlorosilane in a desiccator (33). Silanization was necessary to prevent sticking of the PDMS to the mold. Stamps were prepared by casting PDMS and curing overnight in an oven at 60 °C. All silicon substrates were rinsed with DI-$H_2O$, acetone, and 2-propanol followed by a 20 min UV−ozone cleaning (Jelight 42) prior to use.

**Nanocrystal Monolayer Formation and Pattern Transfer.** Langmuir−Blodgett (LB) films of nanocrystals were assembled using a KSV mini trough system 2 enclosed in a Plexiglas cabinet. Pure DI-$H_2O$ was used as the subphase for all LB studies, and the trough and barriers were thoroughly cleaned with ethanol and rinsed with DI-$H_2O$ before each deposition. Nanocrystals were spread onto the trough using chloroform dispersions of 0.5 mg $mL^{-1}$ FePt nanocrystals or FePt@$SiO_2$ nanoparticles added via a 100 $\mu$L microsyringe (Hamilton). Small droplets were formed at the tip of the syringe and carefully brought into contact with the water surface. Note that, since chloroform is denser than water (34), the droplet size must be small and must be carefully lowered to the water surface to ensure it does not penetrate the surface and sink to the bottom of the trough. Other solvents were tested, but chloroform was found to work very well, due to its volatility and immiscibility with water (35). Depending on the desired nanoparticle loading, a total of 300−600 $\mu$L of the nanocrystal dispersion was added to the trough. After 10 min was allowed for complete evaporation of the solvent, the LB trough was compressed at 10 mm $min^{-1}$ to the desired surface pressure. Surface pressure−area isotherms were recorded using a platinum wilhelmy plate (KSV, 51066) connected to a KSV film balance.

LB nanocrystal films were transferred from the LB trough to silicon substrates by a vertical lift-off procedure. The substrate was dipped vertically below the water surface prior to compressing the film and then, after compressing the film to the desired surface pressure, the substrate was lifted at a rate of 1 mm $min^{-1}$ to transfer the LB film to the substrate. LB films of nanocrystals were transferred to the PDMS stamps by a Langmuir−Schäfer technique in which the stamp was carefully brought into contact horizontally with the water surface (6).

**Materials Characterization.** Transmission electron microscopy (TEM) was performed using either a Phillips EM208 at an accelerating voltage of 80 kV or a JEOL 2010F equipped with a field emission gun operated at 200 kV. The JEOL 2010F TEM is equipped with an Oxford Inca energy dispersive X-ray

spectrometer (EDS), which was used to obtain compositional profiles of the nanocrystals. TEM samples were prepared by drop-casting dilute dispersions of nanoparticles in chloroform onto 200 mesh copper grids (Electron Microscopy Sciences). Scanning electron microscopy (SEM) imaging was performed on nanocrystals deposited on silicon substrates using either LEO 1530 or Zeiss Supra 40 VP SEMs at a working voltage and distance of 10 kV and 3−6 mm. All TEM and SEM images were acquired digitally.

Wide-angle X-ray diffraction (XRD) was performed with a Bruker Nonius D8 Advance powder diffractometer using Cu Kα radiation ($\lambda = 1.54$ Å). For XRD, nanoparticles were deposited onto quartz substrates and scanned for 12 h with a scan rate of 12° min$^{-1}$ at 0.02° increments with a simultaneous sample rotation of 15° min$^{-1}$. Grazing incidence small-angle X-ray scattering (GISAXS) was performed on the D1 line at the Cornell High Energy Synchrotron Source (CHESS). Radiation of wavelength $\lambda = 1.252$ Å with a bandwidth $\Delta\lambda/\lambda$ of 1.5% was used. Scattering patterns were collected on a MedOptics fiber coupled CCD camera with 14-bit dynamic range per pixel (36). Images were background-corrected, and a pedestal value of 20 was added to avoid negative values. The sample to detector distance was 675 mm, as measured by a silver behenate powder standard. The incident angle of the X-ray beam was 0.1°, and images were taken with an exposure time of 5 s. Images were processed using FIT2D (37).

The magnetic properties of the nanocrystals were measured using a superconducting quantum interference device (SQUID, Quantum Design) magnetometer. Typically, magnetization measurements used 5−7 mg of dry nanoparticles placed in a gelatin capsule (Eli Lilly and Co.). Prior to some SQUID measurements, nanoparticles were annealed by heating at 700 °C for 4 h under flowing forming gas (7% $H_2$ 93% $N_2$) inside a 1 in. diameter quartz tube in a Lindberg/Blue M (TF55035A) tube furnace.

Magnetic force microscopy (MFM) and atomic force microscopy (AFM) were performed under ambient conditions at room temperature on a Digital Instruments Multimode Microscope. A CoCr tip magnetized out of the substrate plane was used for MFM (MESP, Veeco). Prior to MFM imaging, the FePt nanocrystal and FePt@$SiO_2$ nanoparticle films were magnetized with an 8 T magnetic field to align the magnetization direction either perpendicular or parallel to the substrate. Separate topography and magnetic phase shift images were obtained by performing first a line scan of the sample topography in TappingMode and then repositioning the tip 60 nm above the sample using Liftmode to measure the magnetic response along the same contour. This procedure was repeated until the entire area had been scanned.

## RESULTS AND DISCUSSION

**Langmuir−Blodgett (LB) Monolayer Formation.** Ordered monolayers of oleic acid/oleylamine (OA/OLA)-stabilized FePt nanocrystals and OTMOS-stabilized FePt@$SiO_2$ nanoparticles were assembled on an LB trough. Figures 1A and 2A show typical surface pressure−area isotherms of the OA/OLA-stabilized FePt and OTMOS-stabilized FePt@$SiO_2$ nanoparticles. The isotherms are qualitatively similar, but the FePt@$SiO_2$ nanoparticle layer was slightly more compressible and required lower surface pressures to obtain ordered monolayers suitable for transfer. The compressibility of the FePt@$SiO_2$ nanoparticle layer was 0.021 ± 0.006 m mN$^{-1}$, compared to 0.005 ± 0.001 m mN$^{-1}$ for the OA/OLA-capped FePt nanocrystal layer (38, 39).

The FePt nanocrystals deposited on the air−water interface initially associate into interconnected strands like those

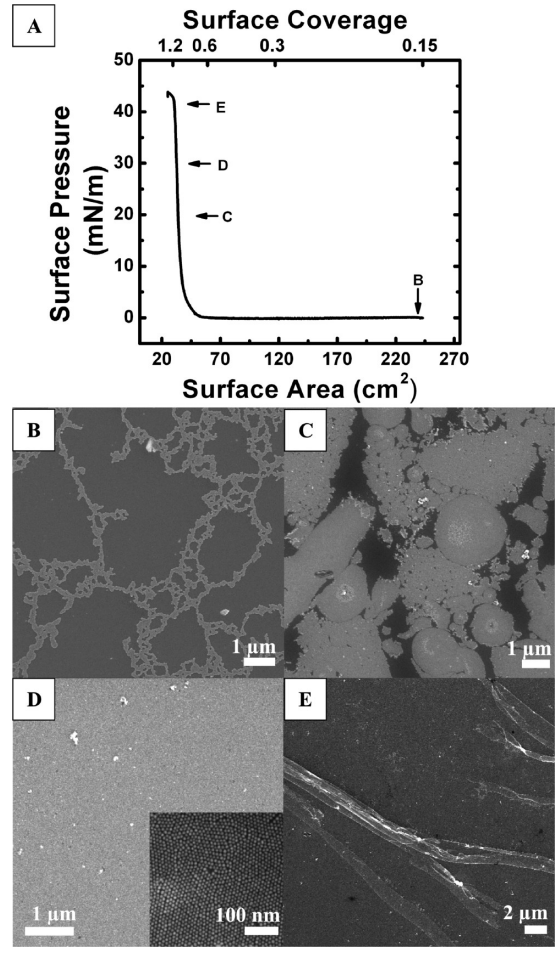


**FIGURE 1. (A) Surface pressure−area isotherm and (B−E) SEM images of an LB film of 6.6 ± 0.6 nm diameter OA/OLA-stabilized FePt nanocrystals. The film was compressed at 10 mm min$^{-1}$. A 0.15 mg portion of FePt nanocrystals was dropped onto an area of 250 cm$^2$. The upper *x* axis denotes the surface coverage of FePt nanocrystals. The SEM samples were prepared by vertically lifting a silicon substrate out of the LB film at the indicated surface pressures. The inset in (D) shows a higher magnification image of the nanocrystal film.**

shown in Figure 1B. Compression reduced the void space between these strands without a measurable increase in surface pressure until the surface area was reduced to 55 ± 3.5 cm$^2$ for the OA/OLA-stabilized FePt nanocrystals and 87 ± 6.0 cm$^2$ for the OTMOS-stabilized FePt@$SiO_2$ nanoparticles, at which point the surface pressure increased significantly. At these surface coverages, the monolayers undergo a phase transition from a low-density gas-like expanded state to a liquid-like compressed monolayer (22). The phase transition corresponds to a surface coverage of 62 ± 3.3% for the OA/OLA-stabilized FePt nanocrystals and 59 ± 4.0% for the OTMOS-stabilized FePt@$SiO_2$ nanoparticles and is consistent with previous observations for gold nanocrystals (23, 40).

FePt@$SiO_2$ nanoparticle films were transferred to PDMS stamps when the pressure was increased to 20 mN m$^{-1}$. Dense close-packed monolayers spanning an entire 1 cm$^2$ silicon substrate (Figure 2B) were obtained at this pressure. The monolayer did, however, exhibit some imperfections, which included particle vacancies, voids approximately

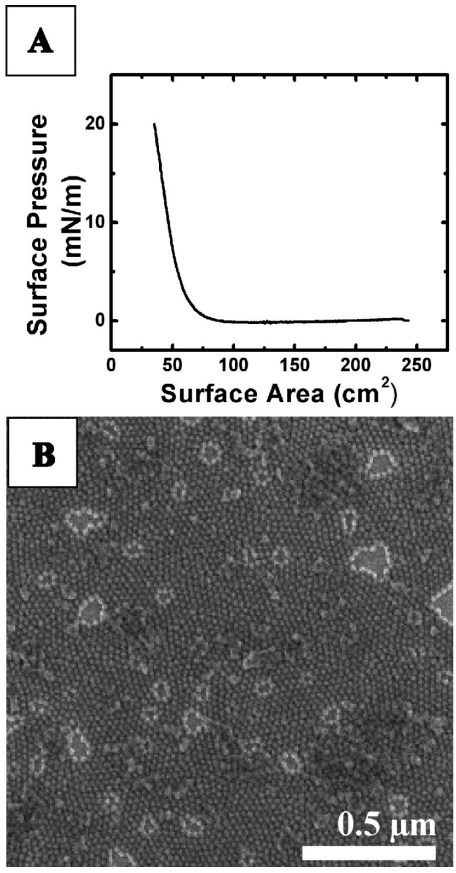


FIGURE 2. (A) Surface pressure−area isotherm and (B) SEM image of a LB film of 25.3 ± 1.8 nm diameter OTMOS-stabilized FePt@$SiO_2$ nanoparticles. The silica shell thickness is 9 nm. A 0.18 mg portion of nanocrystals was deposited onto an area of 250 $cm^2$. The monolayer in (B) was at a surface pressure of 20 mN $m^{-1}$.

100−200 nm in diameter, and some small particle aggregates 100−500 nm in diameter.

The OA/OLA-capped FePt nanocrystals were transferred at a pressure of 30 mN $m^{-1}$. At 20 mN $m^{-1}$, the OA/OLA-capped FePt nanocrystals still exhibited significant voids (1−3 $\mu$m in diameter) in the film (as in Figure 1C), and therefore, the monolayers were further compressed before transfer. At 30 mN $m^{-1}$, the monolayers were virtually free of voids and spanned a 1 $cm^2$ silicon substrate (Figure 1A,D). However, like the FePt@$SiO_2$ nanoparticle films, the OA/OLA-capped FePt nanocrystal monolayers had some imperfections, including particle vacancies and small voids (10−20 nm diameter, corresponding to two to three nanocrystals) residing predominantly at grain boundaries, as well as particle aggregates 30−200 nm in diameter scattered throughout the film (Figure 1D).

Overcompression buckled the FePt nanocrystal films, making them unsuitable for transfer. The OA/OLA-capped nanocrystals buckled at 42 mN $m^{-1}$, corresponding to a plateau in the pressure−area isotherm. Figure 1E shows an SEM of a buckled film with bright bands of nanocrystal bilayers. The bands extend perpendicular to the compression direction. (A higher magnification image of a buckled film is provided in Figure S1 in the Supporting Information).

When excess capping ligand was present in the dispersion, it was impossible to make close-packed monolayers

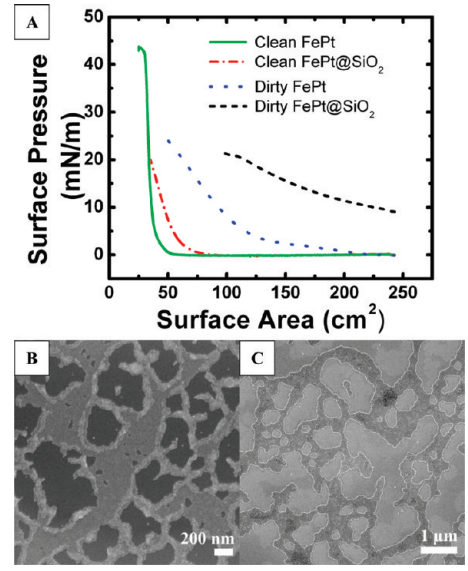


FIGURE 3. (A) Surface pressure−area isotherms and SEM images of OA/OLA-stabilized FePt nanocrystals and OTMOS-stabilized FePt@$SiO_2$ nanoparticles with ("dirty") and without ("clean") residual free capping ligand. "Clean" nanoparticle dispersions were obtained by washing the nanoparticles three times by solvent/antisolvent precipitation and redispersion as described in the Experimental Details. "Dirty" nanoparticle dispersions were those that were washed twice or less or washed three times but then stored for more than 1 week. The SEM images correspond to the "dirty" films of (B) FePt nanocrystals and (C) FePt@$SiO_2$ nanoparticles on silicon substrates transferred by vertical lifting from the LB trough at 25 and 20 mN $m^{-1}$, respectively. The dark regions in (B) and light gray region in (C) are surfactant domains.

of nanoparticles. Free capping ligand partitions to the air−water interface and prevents close packing of the nanoparticles over extended areas and influences the pressure−area isotherms. Figure 3A shows isotherms of nanoparticle monolayers formed with "clean" dispersions (i.e., minimal free capping ligand) and "dirty" dispersions that had a significant amount of free ligand. Clean films had lower starting surface pressures (0−0.5 mN $m^{-1}$) compared to films that had residual ligands (3−9 mN $m^{-1}$) (Figure 3A, dirty FePt@$SiO_2$). The dirty films also exhibited a gradual rise in surface pressure at the start of compression and an early transition to the liquid-like regime (Figure 3A, dirty FePt). Clean monolayers displayed a characteristic flat (~0 mN $m^{-1}$) surface pressure until reaching 55−65% surface coverage and transitioning to the liquid-like region. SEM images (Figure 3B,C) of compressed monolayers with significant free capping ligand revealed pools of surfactant separating domains of ordered nanocrystals. These surfactant domains were typically outlined with a thick multilayer ring of nanocrystals. Meldrum et al. has also reported intervening surfactant domains in their LB films of oleic acid capped silver nanoparticles (41). To alleviate problems caused by free capping ligand, nanoparticles were precipitated and redispersed immediately prior to use to ensure that clean dispersions were spread on the trough (see the Experimental Details). Ligands were found to desorb over time from the nanoparticles when stored as dispersions, and therefore, nanoparticles were always used within 1 week of preparation.

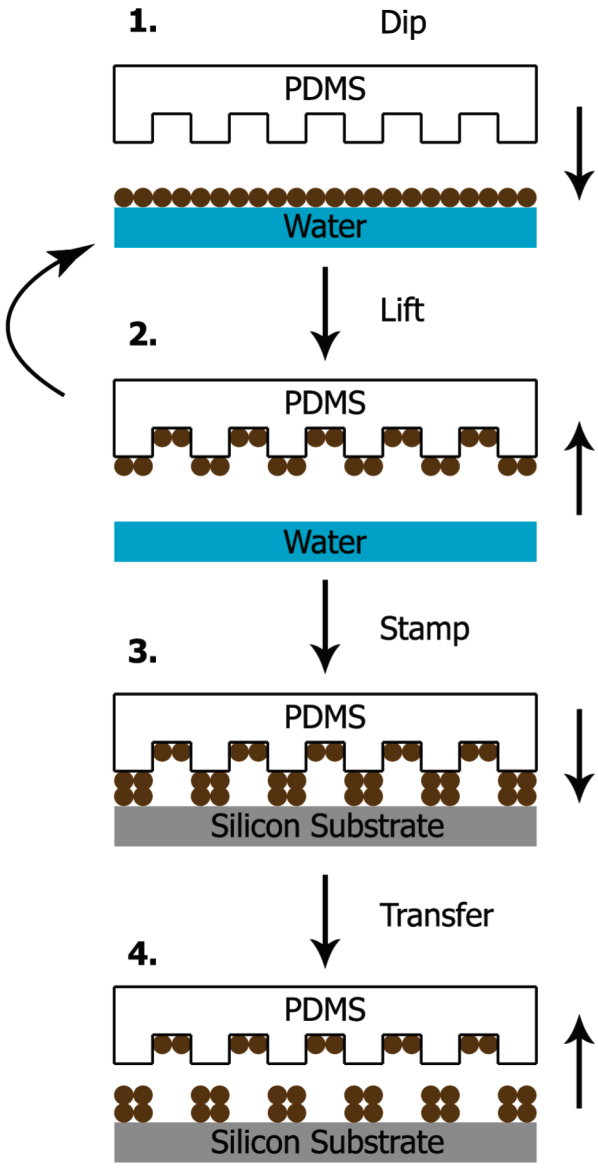


**FIGURE 4. PDMS stamping of nanocrystal monolayers: (1) a patterned PDMS stamp is brought into contact with the LB trough water surface and (2) lifted—the nanoparticles adhere to the PDMS stamp without any special surface treatment; then (3) the inked stamp is contacted with the substrate and held there for ~30 s before (4) lift-off to leave a transferred pattern of nanoparticles on the substrate. Steps 1 and 2 can also be repeated to form a multilayer of nanocrystals that can then be transferred to a substrate (the stamp features and particles are not drawn to scale).**

**Nanoparticle Layer Transfer and Printing.** Nanoparticles were stamped using the process described in Figure 4. The LB monolayer of nanoparticles was transferred to a PDMS stamp patterned with arrays of dots, lines, and squares with 1.5−20 $\mu$m feature sizes and stamped onto a Si substrate. During stamping onto the substrate, care was taken to avoid pressing the raised stamp features onto the substrate. Parts A, B, and D of Figure 5 show SEM images of stamped monolayers of OA/OLA-capped FePt nanocrystals and FePt@$SiO_2$ nanoparticles on Si substrates. The nanoparticles transferred cleanly with feature edge resolutions of approximately 50 nm for the FePt and FePt@$SiO_2$ nanoparticles. Chemical treatment of the substrate was not required.

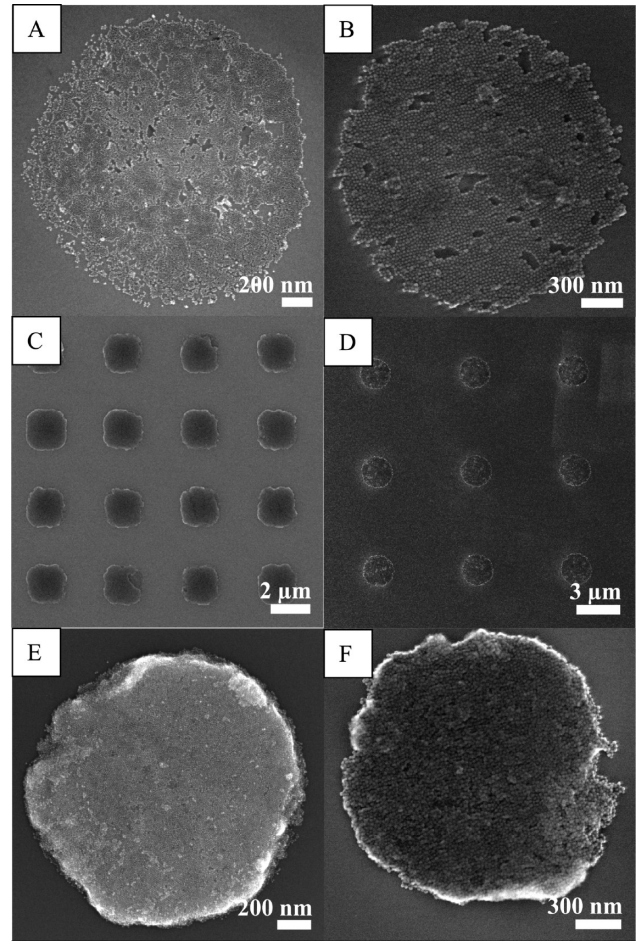


**FIGURE 5. SEM images of PDMS-stamped OA/OLA-capped FePt nanocrystals and OTMOS-stabilized FePt@$SiO_2$ nanoparticles: 1.5 $\mu$m circular features containing monolayers of (A) FePt nanocrystals and (B) FePt@$SiO_2$ nanoparticles, arrays of 1.5 $\mu$m squares of (C) FePt nanocrystal multilayers (6 particles thick) and circles of (D) FePt@$SiO_2$ nanoparticle monolayers, and (E, F) magnified images of 1.5 $\mu$m circular features of an (E) FePt multilayer (four particles thick) and an (F) FePt@$SiO_2$ multilayer (four particles thick). Multilayers were made using stamping method 1.**

Multilayers of FePt nanocrystals and FePt@$SiO_2$ nanoparticles could also be stamped by repeated inking of the PDMS stamp with nanocrystals from the LB trough prior to stamping (method 1) (Figure 4 steps 1 and 2). Patterned multilayers of FePt nanocrystals (one to six monolayers thick) and FePt@$SiO_2$ nanoparticles (one to four monolayers thick) could be printed with good edge resolution and feature uniformity (Figure 5C,E,F). Multilayers could also be transferred by sequentially printing stamps containing one to two layers of nanoparticles (method 2). Figure 8B shows a crossed-line feature made by sequentially stamping two separately inked line stamps at a 90° angle with respect to each other. The nanoparticles adhere to both substrate and underlying nanoparticle layers, without lifting the previous layer of nanoparticles off the substrate. Both methods achieve features of similar uniformity.

GISAXS (42, 43) of a stamped monolayer of OA/OLA-stabilized FePt nanocrystals confirmed the existence of long-range hexagonal order of the nanoparticles in the film. Figure 6 shows a typical GISAXS pattern; sharp Bragg rods and higher order reflections are present, indicating ordered

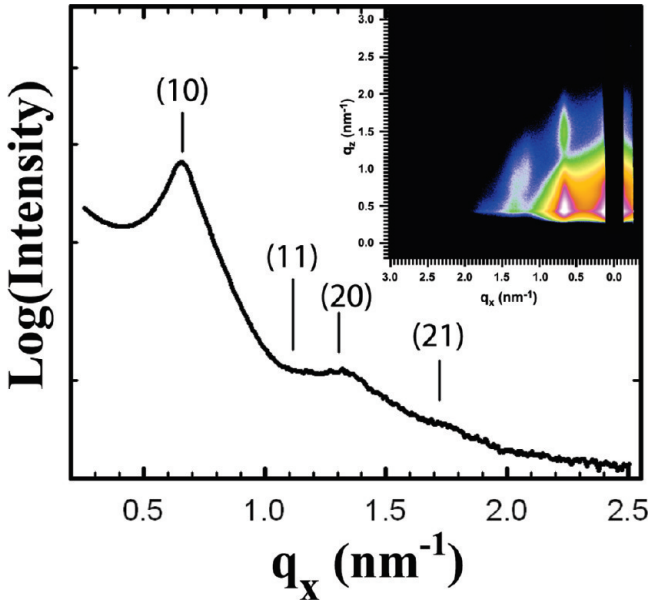


FIGURE 6. GISAXS pattern for a monolayer of PDMS-stamped 6 nm FePt nanocrystals. Inset: scattering intensity measured on the 2D detector (after background correction). The plot is a projection integration onto the *x* axis of the scattering image. The lattice plane indices of a hexagonal monolayer are also indicated.

nanocrystal packing in the film. The ratio of peak positions to the primary peak follows a sequence of 1, $\sqrt{3}$, $\sqrt{4}$, $\sqrt{7}$, indicating hexagonal order, which is consistent with the SEM observations. The first-order scattering peak at $q = 0.65$ nm$^{-1}$ corresponds to the (10) row with a $d$ spacing of 9.6 nm and interparticle spacing of 10.9 nm. This is close to the interparticle spacing of 11.4 nm determined from SEM images. The next two Bragg rods corresponding to the (11) and (20) rows appear to be merged in the projection integration but can be distinctly seen in the GISAXS pattern (Figure 6 inset). This is due to peak broadening caused by the finite size of multiple randomly orientated hexagonally packed grains in the nanocrystal monolayer. The oscillating intensity along the vertical scattering rods is due to the nanocrystal spherical form factor.

**Magnetic Properties of Stamped Nanocrystals.** The stamped FePt nanocrystals and FePt@$SiO_2$ nanoparticles were converted from their as-synthesized random alloy composition to the hard magnetic, compositionally ordered, face-centered tetragonal (fct) $L1_0$ phase by annealing at 700 °C for 4 h under forming gas (7 % $H_2$, 93 % $N_2$) (30). The films were examined by AFM and MFM after annealing. XRD (Figure 7C) confirmed the transformation to the $L1_0$ phase, and SEM showed that the stamped nanocrystal patterns retained their integrity after annealing (Figure 7A,B) with no observable migration of material across the silicon surface. Annealing of the OA/OLA-capped FePt nanocrystals (Figure 7A) led to sintered continuous films of FePt. In contrast, the FePt cores of the FePt@$SiO_2$ nanoparticles (Figure 7B) did not sinter during the annealing process. The silica shell was recently shown to withstand annealing temperatures up to ~850 °C without degradation (30). The AFM images confirmed that the thickness of the stamped features remained

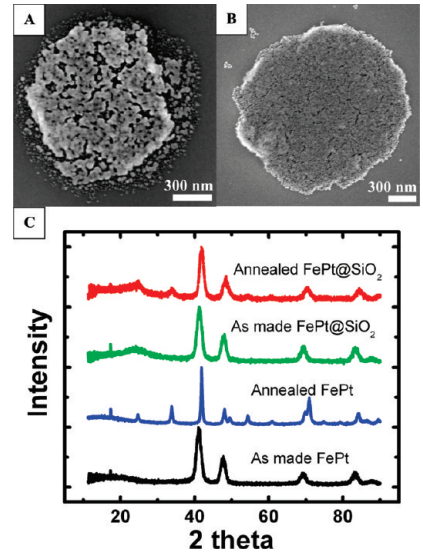


FIGURE 7. SEM images of (A) FePt (six monolayers) and (B) FePt@$SiO_2$ (three monolayers) nanoparticles printed using stamping method 1 onto Si substrates as 1.5 $\mu$m diameter circles after annealing at 700 °C for 4 h under forming gas. (C) XRD of FePt nanocrystals and FePt@$SiO_2$ nanoparticles before and after annealing. For clarity the diffraction peak intensities were normalized by the (111) diffraction peak at $2\theta = 39°$. The slight shifting of the diffraction peaks to higher angle and the emergence of new diffraction peaks at $2\theta$ angles of 53.7 and 60.5° confirm the transition to the tetragonal $L1_0$ phase. The narrowing of the diffraction peaks from the OA/OLA-stabilized FePt nanocrystals is consistent with crystal grain growth and coalescence during annealing. From the observed peak widths, the Scherrer equation (44, 45) was used to estimate the average crystal domain sizes. The uncoated FePt nanocrystals increased in grain size from 5 to 12 nm in diameter and the FePt@$SiO_2$ nanoparticles did not change in size from 5 nm (46).

uniform after the annealing process, revealing only a few small indentations corresponding to cracks in the film.

Magnetic contrast between the annealed FePt features and the diamagnetic silicon substrate was easily visualized by MFM. Figure 8C shows an MFM image of a magnetized feature: the observed negative phase shift of 2.3° corresponds to an attraction between the MFM tip and the sample, indicating permanent magnetization of the FePt film. When the direction of the MFM tip magnetization was reversed, a positive phase shift of 2.3° was observed, corresponding to repulsion between the MFM tip and sample. Thinner films gave a weaker MFM response; for example, a stamped feature only three nanocrystal layers thick (at the same lift height of 60 nm) gave a phase shift of only 0.5°. These MFM measurements showed significantly better magnetic signal uniformity compared to prior MFM measurements of annealed patterned films of Pt@$Fe_2O_3$ core-shell nanoparticles (7).

Figure 8B shows a topographic image of two crossed stripes of FePt@$SiO_2$ nanocrystals. Each stripe is two particle layers thick. AFM line scans showed a uniform height at the intersection that dropped sharply from four to two nanoparticle layers thick at the junction, as expected. This feature geometry conveniently allowed a test of the dependence of the MFM detection resolution on the feature thickness. Figure 8D shows the MFM scan after the feature was magnetized with an external 8 T field out of the plane of the

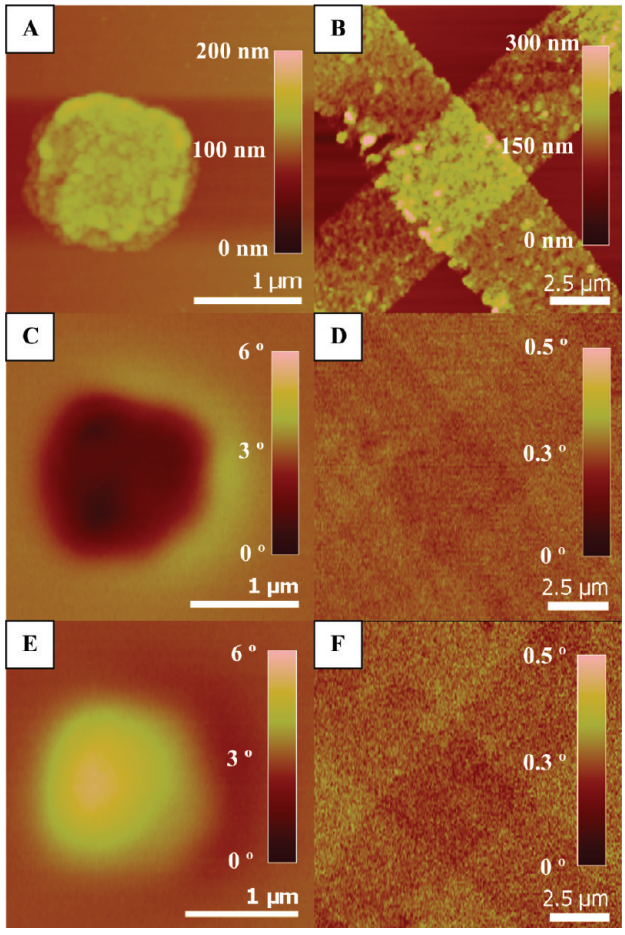


**FIGURE 8. AFM and MFM images of FePt nanocrystals and FePt@$SiO_2$ nanoparticles after annealing. All images were acquired with the MFM tip magnetized out of the plane of the paper at lift height of 60 nm: (A) topographical image of a 1.5 $\mu$m feature of FePt nanocrystals six layers thick made using stamping method 1; (B) crossed-line pattern of stamped FePt@$SiO_2$ nanoparticles four layers thick at the line intersection using stamping method 2; (C, D) MFM images of FePt nanocrystals and FePt@$SiO_2$ nanoparticles corresponding to features in (A) and (B), respectively, after alignment of the magnetic domains out of the plane of the paper; (E, F) MFM images of patterns with similar dimensions to those shown in images (A) and (B), respectively, after alignment of the magnetic domains into the plane of the paper.**

substrate. A faint outline of the feature (corresponding to a negative phase shift of 0.04°) is visible, indicating a weak interaction with the MFM tip. However, after the magnetization of the film was switched, the MFM still measured a negative phase shift of similar magnitude. The reversal of the magnetization direction did not give rise to a positive phase shift as expected, indicating that the MFM response did not result from a magnetic interaction between the tip and the film but was probably a result of van der Waals interactions.

SQUID measurements of the magnetic properties of the FePt@$SiO_2$ nanoparticles showed that they were magnetic at room temperature (Figure 9) and that the lack of MFM signal was not because the sample was not magnetic. The magnetic remanence was 17.7 emu $g^{-1}$ $FePt^{-1}$ for the FePt@$SiO_2$ nanoparticles vs. 28.5 emu $g^{-1}$ $FePt^{-1}$ for the FePt nanocrystals. The annealed printed features are definitely permanent magnets at room temperature, with coercivities of 0.33 T for the FePt@$SiO_2$ nanoparticles and 0.75 T for the sintered FePt nanocrystals. The high coercivity prevents demagnetization, either by heat or in the presence of weak external magnetic field—as emanates from the MFM tip, for example. At 60 nm above the sample, the magnetic field experienced by the sample from the MFM tip is only 33 mT (47), which is well below the coercivity of the FePt nanocrystals and FePt@$SiO_2$ nanoparticles. Since demagnetization by the MFM tip is unlikely, the low MFM signal of the printed FePt@$SiO_2$ nanoparticles results simply from the low magnetic density of the material. FePt makes up only 11% of the total mass of the FePt@$SiO_2$ nanoparticles, which translates to an areal Bohr magneton density of 6.5 $\times$ $10^{14}$ $\mu_B$ $cm^{-2}$ (48). The areal Bohr magneton density of the films of annealed (uncoated) FePt nanocrystals is nearly 2 orders of magnitude higher, at 1.6 $\times$ $10^{16}$ $\mu_B$ $cm^{-2}$. The magnetic field density of the stamped, annealed FePt@$SiO_2$ nanoparticle features is below the detection limit of the MFM tip, though it is measurable for films thicker than 100 nm (46).

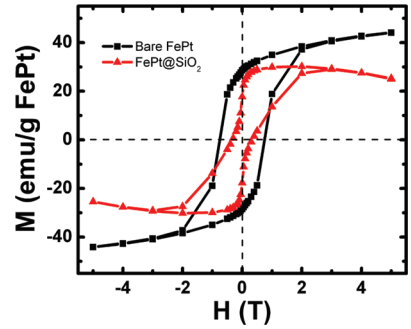


**FIGURE 9. $M-H$ loop for FePt nanocrystals and FePt@$SiO_2$ nanoparticles at room temperature after being annealed at 700 °C for 4 h in forming gas. Magnetization was normalized to a per gram of FePt basis in the sample. A noticeable constriction in the hysteresis loop for FePt@$SiO_2$ was also observed. Zero-field-cooled (ZFC) and field-cooled (FC) scans of the magnetization versus temperature are provided in Figure S2 in the Supporting Information.**

## CONCLUSIONS

In conclusion, FePt nanocrystals and FePt@$SiO_2$ nanoparticles were assembled into close-packed monolayers at the air—water interface of an LB trough and transferred onto silicon substrates using patterned PDMS stamps. The weakly magnetic, as-synthesized, random alloy FePt nanocrystals were converted to the hard magnetic $L1_0$ phase by annealing at 700 °C under forming gas. The patterned features retained their shape and edge resolution after the annealing process and exhibited the properties of permanent magnets at room temperature. MFM could detect at room temperature the magnetization of annealed OLA/OA-capped FePt nanocrystals but not of the stamped and annealed FePt@$SiO_2$ nanoparticles. The low magnetic field strength from the printed FePt@$SiO_2$ nanoparticles was the result of the dilution of the FePt in the silica shells in the layer.

Lowering the measurement temperature, in order to increase the sensitivity of the MFM, or decreasing the silica shell thickness would increase the ferromagnetic response from the FePt@$SiO_2$ nanoparticles to make them detectable

by MFM. Lowering the operating temperature, however, would limit the practicality of implementing FePt@$SiO_2$ nanoparticles in consumer-based magnetic memory storage devices. Alternatively, the scanning Hall probe microscope (47) may be able to image the magnetic properties of the existing films.

**Acknowledgment.** This research was supported by funding from the Robert A. Welch Foundation, the Air Force Research Laboratory (FA8650-07-2-5061), and the National Science Foundation (DMR-0807065). Funding from the W.M. Keck Foundation is also acknowledged. GISAXS measurements were performed at the Cornell High Energy Synchrotron Source (CHESS), which is funded by the National Science Foundation and National Institute of Health/National Institute of General Medical Sciences under NSF awards DMR-0225180 and DMR-0308575.

**Supporting Information Available:** Figures giving additional SEM images and SQUID measurements. This material is available free of charge via the Internet at http://pubs.acs.org.

## REFERENCES AND NOTES

(1) Coufal, H.; Dhar, L.; Mee, C. D. (Eds.) *MRS Bull.* **2006**, *67*.
(2) Wood, R. *J. Magn. Magn. Mater.*, in press.
(3) Lee, Y.; Choi, J.-r.; Lee, K. J.; Stott, N. E.; Kim, D. *Nanotechnology* **2008**, *19*, 415604.
(4) Schulz, D. L.; Pehnt, M.; Rose, D. H.; Urgiles, E.; Cahill, A. F.; Niles, D. W.; Jones, K. M.; Ellingson, R. J.; Curtis, C. J.; Ginley, D. S. *Chem. Mater.* **1997**, *9*, 889–900.
(5) Guo, Q.; Teng, X.; Rahman, S.; Yang, H. *J. Am. Chem. Soc.* **2003**, *125*, 630–631.
(6) Santhanam, V.; Andres, R. P. *Nano Lett.* **2004**, *4*, 41–44.
(7) Guo, Q.; Teng, X.; Yang, H. *Adv. Mater.* **2004**, *16*, 1337–1341.
(8) Park, J.-I.; Lee, W.-R.; Bae, S.-S.; Kim, Y. J.; Yoo, K.-H.; Cheon, J.; Kim, S. *J. Phys. Chem. B* **2005**, *109*, 13119–13123.
(9) Loo, Y.-L.; Willett, R. L.; Baldwin, K. W.; Rogers, J. A. *Appl. Phys. Lett.* **2002**, *81*, 562–564.
(10) Felmet, K.; Loo, Y.-L.; Sun, Y. *Appl. Phys. Lett.* **2004**, *85*, 3316–3318.
(11) Richter, H. J.; Harkness, S. D. I. *MRS Bull.* **2006**, *31*, 384–388.
(12) Weller, D.; Moser, A. *IEEE Trans. Magn.* **1999**, *35*, 4423–4439.
(13) Jeong, U.; Teng, X.; Wang, Y.; Yang, H.; Xia, Y. *Adv. Mater.* **2007**, *19*, 33–60.
(14) Chen, M.; Liu, J. P.; Sun, S. *J. Am. Chem. Soc.* **2004**, *126*, 8394–8395.
(15) Sun, S.; Murray, C. B.; Weller, D.; Folks, L.; Moser, A. *Science* **2000**, *287*, 1989–1992.
(16) Chen, M.; Nikles, D. E. *J. Appl. Phys.* **2002**, *91*, 8477–8479.
(17) Ely, T. O.; Pan, C.; Amiens, C.; Chaudret, B.; Dassenoy, F.; Lecante, P.; Casanove, M. J.; Mosset, A.; Respaud, M.; Broto, J. M. *J. Phys. Chem. B* **2000**, *104*, 695–702.
(18) Vossmeyer, T.; Jia, S.; DeIonno, E.; Diehl, M. R.; Kim, S. H.; Peng, X.; Alivisatos, A. P.; Heath, J. R. *J. Appl. Phys.* **1998**, *84*, 3664–3670.
(19) Mendes, P. M.; Jacke, S.; Critchley, K.; Plaza, J.; Chen, Y.; Nikitin, K.; Palmer, R. E.; Preece, J. A.; Evans, S. D.; Fitzmaurice, D. *Langmuir* **2004**, *20*, 3766–3768.
(20) Lopes, W. A.; Jaeger, H. M. *Nature* **2001**, *414*, 735–738.
(21) Chen, C.-F.; Tzeng, S.-D.; Lin, M.-H.; Gwo, S. *Langmuir* **2006**, *22*, 7819–7824.
(22) Heath, J. R.; Knobler, C. M.; Leff, D. V. *J. Phys. Chem. B* **1997**, *101*, 189–197.
(23) Huang, S.; Tsutsui, G.; Sakaue, H.; Shingubara, S.; Takahagi, T. *J. Vac. Sci. Technol.* **2001**, *19*, 2045–2049.
(24) Li, X.; Zhang, L.; Wang, X.; Shimoyama, I.; Sun, X.; Seo, W.-S.; Dai, H. *J. Am. Chem. Soc.* **2007**, *129*, 4890–4891.
(25) Yang, P.; Kim, F. *ChemPhysChem* **2002**, *3*, 503–506.
(26) Whang, D.; Jin, S.; Wu, Y.; Lieber, C. M. *Nano Lett.* **2003**, *3*, 1255–1259.
(27) Tao, A.; Sinsermsuksakul, P.; Yang, P. *Nat. Nanotechnol.* **2007**, *2*, 435–440.
(28) Santhanam, V.; Liu, J.; Agarwal, R.; Andres, R. P. *Langmuir* **2003**, *19*, 7881–7887.
(29) Xia, Y.; McClelland, J. J.; Gupta, R.; Qin, D.; Zhao, X. M.; Sohn, L. L.; Celotta, R. J.; Whitesides, G. M. *Adv. Mater.* **1997**, *9*, 147–149.
(30) Lee, D. C.; Mikulec, F. V.; Pelaez, J. M.; Koo, B.; Korgel, B. A. *J. Phys. Chem. B* **2006**, *110*, 11160–11166.
(31) Wang, W.; Gu, B.; Liang, L.; Hamilton, W. *J. Phys. Chem. B* **2003**, *107*, 3400–3404.
(32) Kumar, A.; Whitesides, G. M. *Appl. Phys. Lett.* **1993**, *63*, 2002.
(33) Yang, H.; Deschatelets, P.; Brittain, S. T.; Whitesides, G. M. *Adv. Mater.* **2001**, *13*, 54–58.
(34) Sanni, S. A.; Hutchison, P. *J. Chem. Eng. Data* **1973**, *18*, 317–22.
(35) Huang, S.; Tsutsui, G.; Sakaue, H.; Shingubara, S.; Takahagi, T. *J. Vac. Sci. Technol.* **2001**, *19*, 115–120.
(36) Gruner, S. M.; Tate, M. W.; Eikenberry, E. F. *Rev. Sci. Instrum.* **2002**, *73*, 2815–2842.
(37) Hammersley, A. P. ESRF Internal report 1997, ESRF97HAO2T.
(38) The compressibility $C = -(1/a)(\partial a/\partial \Pi)_{T,P,n_i}$, where $a$ is surface area per particle and $\Pi$ is the surface pressure.
(39) These compressibility values are determined for films at 75% of the optimal dipping surface pressure surface pressure (15 mN $m^{-1}$ FePt@$SiO_2$ nanoparticles and 22.5 mN $m^{-1}$ FePt nanocrystals).
(40) The surface coverage was calculated by taking the area occupied by a hexagonal close-packed film of nanoparticles based on the mass of the sample deposited on the surface of the trough and dividing it by the area of the trough at a given point. The weight of capping ligand was accounted for as well by assuming 80% coverage of the nanoparticle surface. For the case of bare FePt nanocrystals, we assumed a 50/50 coverage of oleic acid and oleylamine. Ligand lengths were based on reported values.
(41) Meldrum, F. C.; Kotov, N. A.; Fendler, J. H. *Langmuir* **1994**, *10*, 2035–40.
(42) Smilgies, D.-M.; Busch, P.; Posselt, D.; Papadakis, C. M. *Synchrotron Radiation News* **2002**, *15*.
(43) Saunders, A. E.; Ghezelbash, A.; Smilgies, D.-M.; Sigman, M. B.; Korgel, B. A. *Nano Lett.* **2006**, *6*, 2959–2963.
(44) Chung, D. *X-ray Diffraction at Elevated Temperatures: a Method for In Situ Process Analysis*; VCH: Weinheim, Germany, 1992.
(45) The full width at half-maximum $B$ of the diffraction peaks is related to the crystal domain size $L$ in the Scherrer equation by $L = 0.9\lambda/(B \cos \theta)$, where $\lambda$ is the X-ray wavelength and $\theta$ is the diffraction angle.
(46) Hyun, C.; Lee, D. C.; Korgel, B. A.; de Lozanne, A. *Nanotechnology* **2007**, *18*, 055704.
(47) Kweon, S.; Samarth, N.; Lozanne, A. d. *J. Appl. Phys.* **2009**, *105*, 093906.
(48) The areal Bohr magneton density is estimated from the magnetization measured at 300 K. The number of particles per area was calculated by assuming an HCP monolayer of nanoparticles.

AM900237D